CRYSTAL GROWTH & DESIGN

pubs.acs.org/crystal

Article

Perturbation of the Classic Binary Adduct C_6H_6:C_6F_6 by Chlorine Substitution

Joseph C. Bear, Ronen E. Ghosh, and Jeremy K. Cockcroft*

Cite This: *Cryst. Growth Des.* 2024, 24, 3021−3029

Read Online

ACCESS | Metrics & More | Article Recommendations | Supporting Information

ABSTRACT: This paper presents a comprehensive exploration of the impact of monochlorine substitution on the solid-state phases of the classic binary adduct C_6H_6:C_6F_6. Crystal structures for all four phases of C_6H_6:C_6F_5Cl were determined using single-crystal X-ray diffraction, with complementary data from differential scanning calorimetry (DSC) and variable-temperature powder X-ray diffraction (VT-PXRD). The study reveals that phases I and III would have been overlooked without the additional information provided by DSC and PXRD. Symmetry changes during the phase transitions, including the loss of 3-fold and mirror symmetry, are crucial for our understanding of the observed transformations. Comparisons with the prototype C_6H_6:C_6F_6, the methyl-substituted $C_6H_5CH_3$:C_6F_6 and iodine-substituted analogue C_6H_6:$(C_6F_5I)_2$ provide useful insights into the noncovalent interactions holding these cocrystals together. The experimental results herein may be useful for informing crystal structure prediction, especially in distinguishing between structures of similar energy.

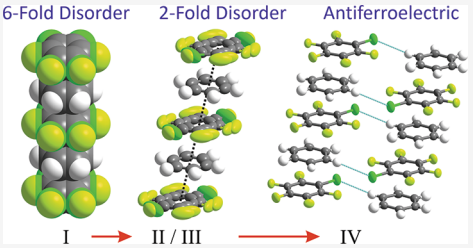

INTRODUCTION

Crystal structure prediction (CSP) has advanced rapidly since the first CCDC-organized round robin at the turn of the century,[1] with the results of the seventh blind test published in 2016[2] and the latest blind test presented orally by Hunnisett at the ACA Meeting in 2022, and then at the BCA Spring Meeting and 26th IUCr Congress, both in 2023.[3] CSP has enabled the crystal structures of relatively large organic molecules, such as those used in the pharmaceutical industry, to be predicted with ever increasing degrees of accuracy. In recent years, the field of CSP has expanded from small organic molecules to complex metal−organic frameworks[4] and supramolecular solids.[5] However, significant challenges still remain.[6,7] First, the minimum-energy landscapes encountered in CSP frequently predict many structures of similar energy and density.[8] Nearly all experimentally known crystal polymorphs lie within 10 kJ mol^{-1} of one another, and, for around 90% of cases, the energy differences between them is less than 4 kJ mol^{-1}.[9] Second, CSP often focuses on the prediction of structures at 0 K whereas in reality, entropy and thermal vibrational motion of the atoms may be crucial in determining the lowest-energy form.[10] Finally, the vast majority of CSP research has focused on the thermodynamically stable forms but polymorph formation is frequently influenced by kinetic factors, making the identification of the thermodynamically most stable form harder to identify.[6]

These challenges are being addressed using a wide variety of strategies. A recent proposed improvement to CSP is the use of quantum mechanical calculations for molecular dimers, using an accurate two-body, rigid-monomer *ab initio*-based force field (aiFF) to build up possible crystal structures in contrast to the use of traditional empirical force fields.[11] An alternative approach, developed McDonagh et al.,[12] used machine learning to improve force-field lattice-energy calculations by more accurately predicting corrections to two-body interactions with a higher level of theory in a fragment-based approach. Machine learning is now seen as computationally cheap and flexible enough to be deployed within existing CSP methods to both reduce the search space and rank crystal structure candidates.

While the modeling of the temperature-dependent properties of organic molecular crystals are being developed,[13] drawbacks still remain for systems with phase transitions and/or dynamic disorder, especially as over 20% of polymorphic structures are predicted to be enantiotropic.[14] The consideration of prenucleation clusters has been suggested by Carpenter and Grünwald as a way of incorporating kinetic effects into existing methods of CSP as an aid to discovering the most likely metastable polymorphic forms.[15] Interestingly, while most CSPs have focused on organic molecules, a recent study has attempted CSP on inorganic oxides related to materials in the Earth (and also an alloy) for which non-0 K methods were required for the prediction of phases that form under nonambient conditions.[16]

Hand-in-hand with CSP progress are the developments in experimental structure determination, which has led to a

Received: January 29, 2024
Revised: March 8, 2024
Accepted: March 8, 2024
Published: March 22, 2024

https://doi.org/10.1021/acs.cgd.4c00134
Cryst. Growth Des. 2024, 24, 3021−3029

massive increase in available experimental crystallographic data as shown by the exponential growth of, for example, the Cambridge Structural Database at CCDC.[17,18] Advances in laboratory X-ray sources (focused beams), X-ray detection (hybrid-pixel detectors), computer processing power and graphics, bespoke crystallographic software for real-time data reduction, and crystal structure solution have all contributed to rapid advancements in methodology. In particular, the crystal structures of solid-state phases which were previously inaccessible are now amenable to rapid structure solution, especially when combined with complementary techniques.[19]

Despite the discovery over 60 years ago of one of the simplest organic cocrystals containing molecules without "classical" hydrogen bonding,[20] namely, the 1:1 adduct of benzene (C_6H_6) and hexafluorobenzene (C_6F_6), the study of noncovalent interactions has only recently sparked mainstream interest,[21,22] particularly with the recognition by IUPAC of the halogen bond,[23,24] and with a recent series of international conferences themed around noncovalent interactions (held in Lisbon, 2019; Strasbourg, 2022; and proposed for Belgrade, 2024).[25] Although a number of derivative structures of C_6H_6:C_6F_6 were determined in the pioneering work by Dahl et al. during the 1970s,[26−28] it took a further 3 decades from the discovery of C_6H_6:C_6F_6 for the structure of its lowest-temperature form, namely, phase IV, to be determined.[29] The structure solution demonstrated that the stacking interactions of the rings in this adduct matched that expected for molecules with opposite quadrupole moments.[30,31] In the early 1990s, it was necessary to use data from both synchrotron X-ray and neutron powder diffractometers, an approach that was, in itself, a novel development at that time. This enabled the structure of phase IV at 1.5 K to be solved and refined using a deuterated sample of C_6H_6. In addition, powder diffraction patterns of the higher-temperature phases I, II, and III were identified and indexed. By 2018, the availability of laboratory variable-temperature powder X-ray diffraction (VT-PXRD), low-temperature differential scanning calorimetry (DSC), micro-focus X-ray sources for single-crystal diffraction (SXD), all combined with powerful desktop computers and user-friendly crystallographic software enabled the structures of phases I to III of C_6H_6:C_6F_6 to be determined and refined for the first time.[32]

Armed with these new modern tools, the question was raised of whether we could extend the studies on columnar structures further. Initially, our investigation focused on studying the influence of methyl substitution on the C_6H_6 ring in this type of cocrystal,[33] before examining the effect on molecular stacking of substituting ferrocene for benzene, as both have no dipole but have similar quadrupole moments.[34] The effect on the dynamics of the $Fe(C_5H_5)_2$ molecules was quite remarkable with the order−disorder transition temperature in $Fe(C_5H_5)_2$ being changed by over 100 K.

This led us to pose the question: how would fluorine substitution by chlorine in C_6F_6 perturb the noncovalent interactions in the prototype adduct C_6H_6:C_6F_6? In addition, this raises the interesting question of how many phases might be observed in a cocrystal formed by C_6H_6 and C_6F_5Cl compared to the four observed in the prototype. With methyl substitution for H in the prototypical material, three solid-state phases are observed for the 1:1 adducts $C_6H_5CH_3$:C_6F_6 and *p*-$C_6H_4(CH_3)_2$:C_6F_6 but only the toluene adduct was seen to exhibit the same "plastic"[35] (i.e., highly orientationally disordered) rhombohedral phase seen in C_6H_6:C_6F_6.[32] Based on the toluene adduct, $C_6H_5CH_3$:C_6F_6, we suspected that a 1:1 adduct of C_6H_6 and C_6F_5Cl coformers might exhibit at least three solid-state phases on cooling to low temperature. As far as we know, current state-of-the-art CSP methods cannot reliably determine the structures of dynamically disordered phases, let alone how many might exist at ambient pressure.[36]

There are a couple of interesting studies on the noncovalent interactions of C_6F_5Cl with flat molecules in which 1:1 cocrystal columnar structures are formed. Pang et al. investigated adducts of pyrene ($C_{16}H_{10}$) with halopentafluorobenzenes (X = F, Cl, Br, I).[37] The columnar structures formed by the adducts $C_{16}H_{10}$:C_6F_6 and $C_{16}H_{10}$:C_6F_5Cl are very similar but the use of C_6F_5Cl results in a columnar structure in which alternate molecules of C_6F_5Cl are ordered in an antiferroelectric arrangement. By contrast, Rozhkov et al. exploited electron-rich d^8 transition metal square-planar complexes, namely, $Pd(acac)_2$ and $Pt(acac)_2$, to form adducts with the pi-hole molecules C_6F_6 and C_6F_5Cl.[38] In these novel columnar structures, antiferroelectric ordering of the C_6F_5Cl molecule was not reported.

We note that there has been other interest in the noncovalent interactions of benzene with halogen-containing organic molecules. In particular, Bujak et al.[39] studied the cocrystal formed by CF_3I with benzene where the molecular components are held together by a halogen bond, C−I···π(C_6H_6), as well as by C−H···π(C_6H_6) and H···F interactions. The halogen-bond interaction results in a cocrystal in which two molecules of CF_3I interact with each face of a single C_6H_6 molecule to form C_6H_6:$(CF_3I)_2$. Their study was extended to the interactions between benzene and pentafluoroiodobenzene,[40] where a cocrystal is formed in the ratio 1:2 again (*i.e.* one molecule of C_6H_6 to two of C_6F_5I) but, in marked contrast to C_6H_6:$(CF_3I)_2$, the C−I···π(C_6H_6) interactions are absent.

In the structure of C_6H_6:$(C_6F_5I)_2$, the molecules are stacked alternately in columns with the C_6F_5I molecules antiferroelectric arranged in pairs within the column and with the rings slightly tilted with regard to the column axis (see Figure S1), as seen also in adducts we have studied.[19,32−34,41] In addition, the relatively large size of the iodine atom results in C_6H_6 and C_6F_5I molecules not being perfectly coplanar to each other within a column, but with an interplanar angle of about 9.5°. Pairs of antiferroelectrically arranged C_6F_5I molecules are coplanar by symmetry. Furthermore, to satisfy intercolumnar interactions, adjacent columns are tilted alternately with each other, resulting in the $P2_1/c$ space-group symmetry for phase I of this adduct. Thus, the arrangement of molecules in the crystal structure of C_6H_6:$(C_6F_5I)_2$ is not based on a simple alternating stack of component molecules as in other systems that we have studied. Finally, only two phases are reported, namely, a monoclinic phase I and a slight triclinic distortion of it, assigned as phase II. This study by Bujak et al.[40] leads to two interesting questions: would a cocrystal formed by C_6H_6 and C_6F_5Cl exist as 1:1 as in the prototype (and various derivatives) or would it exist as 1:2 as in C_6H_6:$(C_6F_5I)_2$; second, how many phases might be observed (assuming that a cocrystal of C_6H_6 and C_6F_5Cl forms) given that F substitution by Cl in C_6F_6 is not expected to make a large change to the surface flatness of the C_6F_6 ring in contrast to substitution by I in C_6F_5I?

https://doi.org/10.1021/acs.cgd.4c00134
Cryst. Growth Des. 2024, 24, 3021−3029

EXPERIMENTAL SECTION

A sample of C_6H_6:C_6F_5Cl was prepared from the pure components with our assumption that the most likely adduct to be formed would be one with a 1:1 stoichiometry. DSC data were measured on C_6H_6:C_6F_5Cl over the temperature range 100 to 300 K. VT-PXRD data were collected initially from 100 to 280 K in 10 K steps. Measurements were repeated in 5 K steps on heating for the temperature range 150 to 185 K. Finally, to probe for the existence of a high-temperature plastic phase, VT-PXRD data were obtained from 260 to 270 K in 2 K steps. No significant differences in recorded temperatures were evident between the techniques. Further details of the materials used and the DSC and VT-PXRD experiments are given in the Supporting Information.

For the single-crystal experiments, a narrow capillary containing C_6H_6:C_6F_5Cl was mounted on the SXD instrument, and the sample was frozen to form a polycrystalline material. The sample was then warmed to just below the melt to anneal into larger crystals and slowly recooled to 260 K and then 200 K. These temperatures were chosen based on the knowledge of the system gleaned from the DSC and VT-PXRD measurements. A full sphere of data was collected at 200 K in less than 1 h. The sample was then cooled to 165 K, but the software still identified the unit cell as monoclinic, so it was cooled down further to 125 K and a second full sphere of data was collected. The sample was allowed to melt overnight. Next day, the sample was cooled to just below the melt to grow crystals and then a full sphere of data was collected at 160 K. Finally, the same sample was melted and annealed at 262 K with data being collected for a significantly longer period of time. Further details of the SXD experiments are provided in the Supporting Information.

RESULTS

The DSC data, displayed in Figure 1, showed remarkable reproducibility on cycling through multiple cooling and heating cycles, the only noticeable difference being the temperature for the sudden onset of freezing (Figure S2). The enthalpy of fusion is 7.82 kJ mol^{-1} and the corresponding enthalpy of solidification is −7.83 kJ mol^{-1}. For the three solid-state phase transitions (IV to III, III to II, and II to I), the enthalpies of transition on heating are 0.73, 0.29, and 3.95 kJ mol^{-1}, respectively; the corresponding values on cooling are of similar magnitude (−0.70, −0.29, and −3.70 kJ mol^{-1}, respectively). On heating, we observed a reproducible weak peak, visible at 229 K, which cannot be explained in terms of the solid-state phase transitions seen in variable-temperature powder X-ray diffraction data, and with no equivalent peak seen on cooling.

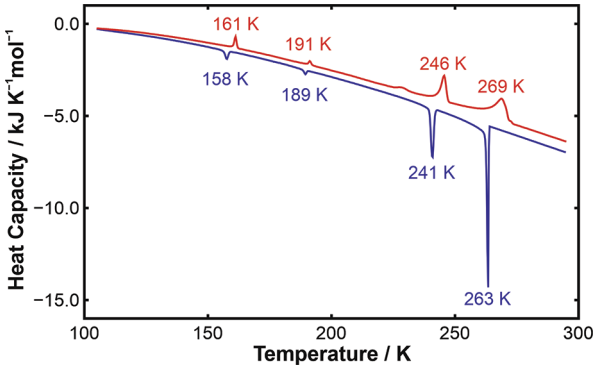

Figure 1. Differential scanning calorimetry data obtained on cooling (in blue) and heating (in red) for a sample of C_6H_6:C_6F_5Cl. Multiple solid-state phase transitions were evident below the melt at 269 K. On cooling below the freezing transition at 263 K, transitions were observed between: phases I and II at 241 K, phases II and III at 189 K, and phases III and IV at 158 K. On heating, equivalent transitions were observed at 161 (IV to III), 191 (III to II), and 246 K (II to I).

The VT-PXRD data showed only three solid-state phases initially with phase I, which only exists over a narrow range of temperature, being unobserved due to the 10 K step size used. The existence of four solid-state phases under ambient pressure was confirmed with the use of a smaller step size in temperature (Figure 2 and Figure S3). The absence of strong peaks in the VT-PXRD data for either pure C_6H_6 or pure C_6F_5Cl demonstrated that a 1:1 adduct had been formed from the melt in-line with our initial sample preparation assumption and subsequently proved by SXD. Data analysis using the PXRD indexing package Crysfire2020[42] identified a monoclinic cell for phase II and triclinic cells for phases III and IV, with the primitive cell for phase IV having twice the volume of the primitive unit cell for phase III (Table S1). The success of the indexing software can be seen in the high figures of merit (see M_{20} in Table S1) and the excellent match with the calculated peak positions for the suggested cells (see Figure S4a,b). It should be noted that, despite all of the first 20 lines being indexed for each phase, the VT-PXRD patterns for each of phases II, III, and IV exhibited a very weak peak at about $2\theta \approx 19.8°$ (highlighted with the green arrow in Figure S4a,b). This very weak peak is attributed to the strongest diffraction peak of solid benzene and, consequently, was deliberately omitted from all of the indexing attempts.

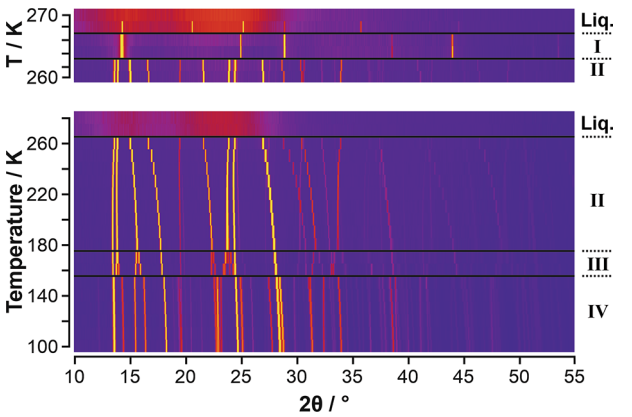

Figure 2. Variable-temperature PXRD data obtained on heating in 2 K steps (top) and 10 K steps (bottom) for a sample of C_6H_6:C_6F_5Cl. The data are shown as a color surface plot where the range of intensity is shown as a sequential color scale, from low counts in dark blue via intermediate counts in red, to high counts in yellow. Three solid-state phases, labeled II, III, and IV, are clearly seen in the bottom plot. With the finer 2 K step in temperature, an additional phase, labeled I, was observed just below the melt (top). As with other related adducts, a liquid "structure" is seen in the liquid state in the form of the double hump in the PXRD patterns.

Following indexing of the VT-PXRD data, whole-pattern fitting using the LeBail method[43] was used to obtain unit-cell parameters and unit-cell volumes at each measured temperature, enabling molecular volume as a function of temperature to be obtained. Exemplar LeBail fits are shown in Figure S4c,d. The variation of molecular volume with temperature is shown in Figure 3 with the changes in unit-cell parameters with temperature shown in Figure S5. There is a clear jump in volume at the I−II (*ca.* 1%) and III−IV (*ca.* 2%) phase transitions, but there is no appreciable change in molecular volume at the II−III transition. This is consistent with the II−

https://doi.org/10.1021/acs.cgd.4c00134
Cryst. Growth Des. 2024, 24, 3021−3029

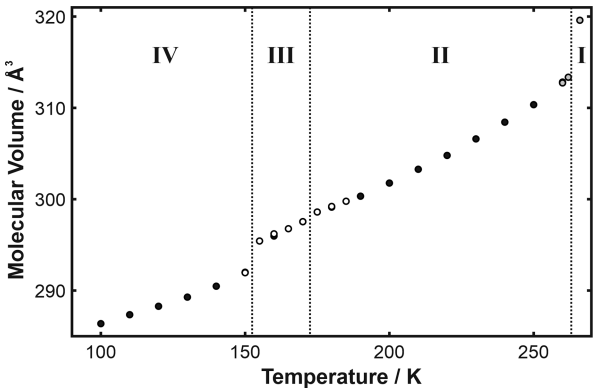

Figure 3. Molecular volume as a function of temperature was obtained by dividing the unit cell volume from the PXRD data by the number of molecules of C_6H_6:C_6F_5Cl per unit cell. Note that the PXRD data for phase I exhibited only *hk*0 reflections, so the molecular volume shown here for phase I is the sole value obtained from the SXD experiment at 262 K.

III transition involving a subtle distortion of the structure but without any change in the degree of disorder of the C_6F_5Cl molecules (as determined by SXD).

The crystal structures of all 4 phases of C_6H_6:C_6F_5Cl were determined using the multigrain approach described in our earlier work, *i.e.*, no attempt was made to grow one perfect single-crystal but rather just large crystals are grown from the melt in the X-ray capillary.[19] For this molecular system, crystals of C_6H_6:C_6F_5Cl were initially produced in phase II. However, we would not have known this without recourse to the indexed VT-PXRD data, the knowledge of which proved to be crucial for all of the SXD experiments. After structure solution and measurement of data on phase II, the crystals were cooled stepwise, but the SXD acquisition software kept suggesting a monoclinic cell until we had taken the sample below 150 K, at which point the pattern of spots on the SXD detector changed noticeably. Structure solution for data collected at 125 K using a primitive triclinic cell showed that we were in phase IV based on our VT-PXRD data.

The experiment was repeated on the same sample the next day with the intention of collecting data on phases I and III. The sample was cooled to 160 K with the aim of measuring phase III. Unit-cell indexing of a small number of frames measured by SXD at this temperature frequently found an *I*-centered monoclinic cell similar to that of phase II, whereas the correct cell for phase III is one that is a small triclinic distortion of the phase II monoclinic cell. This can be easily missed (as happened to us initially) when SXD is the only technique being used. By contrast, PXRD (with its higher 2θ resolution) is much more sensitive than SXD to small unit-cell distortions, which lead to splitting of the peaks in 2θ. In this case, the *I*-centered triclinic cell used to describe phase III at 160 K has unit-cell angles where α is approximately equal to 91° and γ is close to 92° (see Table S2). Both of these values are sufficiently close to 90° for the SXD software to suggest an *I*-centered monoclinic cell when only a few frames of data are measured in the screening scans.

Finally, several attempts were made to obtain data on phase I. Growing crystals of phase I is straightforward as they grow readily inside the capillary at temperatures just below the melt. (The crystals tend to grow such that {001} is parallel to the

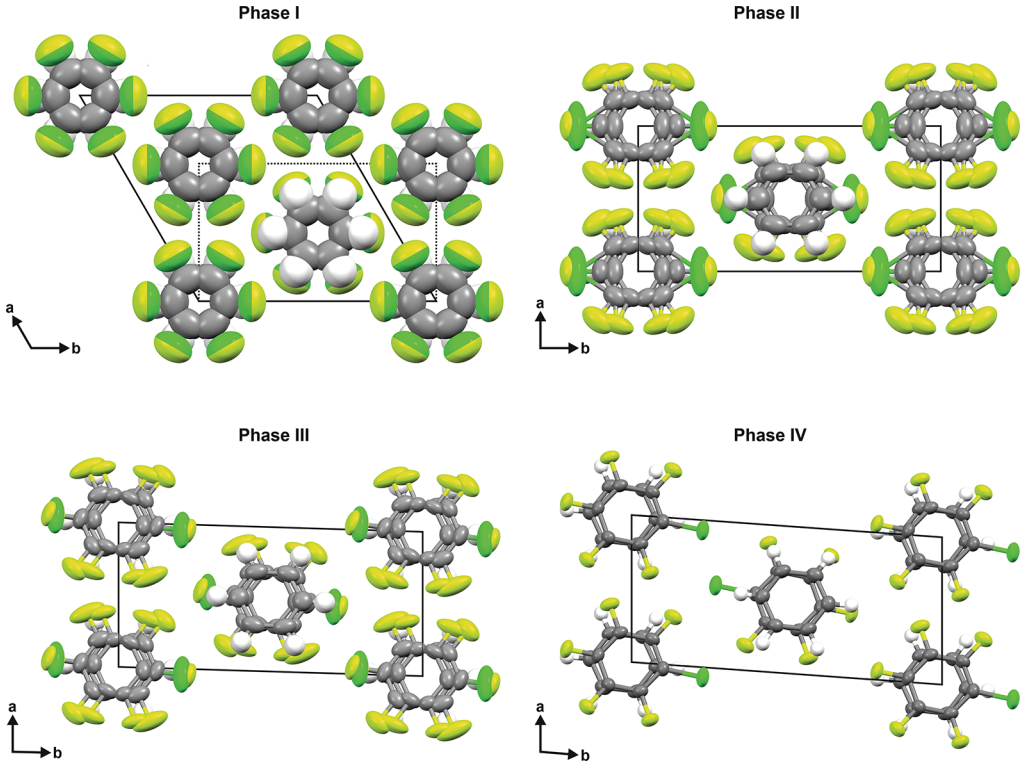

Figure 4. Views of the crystal structures of C_6H_6:C_6F_5Cl in phases I, II, III, and IV viewed along **c**, the column axis of the stacked molecules. F atoms are shown in light green, Cl atoms in midgreen, C atoms in midgray, and H atoms in white. The figure shows how decreasing the sample temperature reduces the thermal disorder of the molecules and, at the same time, lowers the symmetry of the crystal structures. In phases II and III with 2-fold disorder of the C_6F_5Cl molecules, the Cl atom is seen as the "inner" atom and the fluorine opposite it in the ring as the "outer" one.

https://doi.org/10.1021/acs.cgd.4c00134
Cryst. Growth Des. 2024, 24, 3021−3029

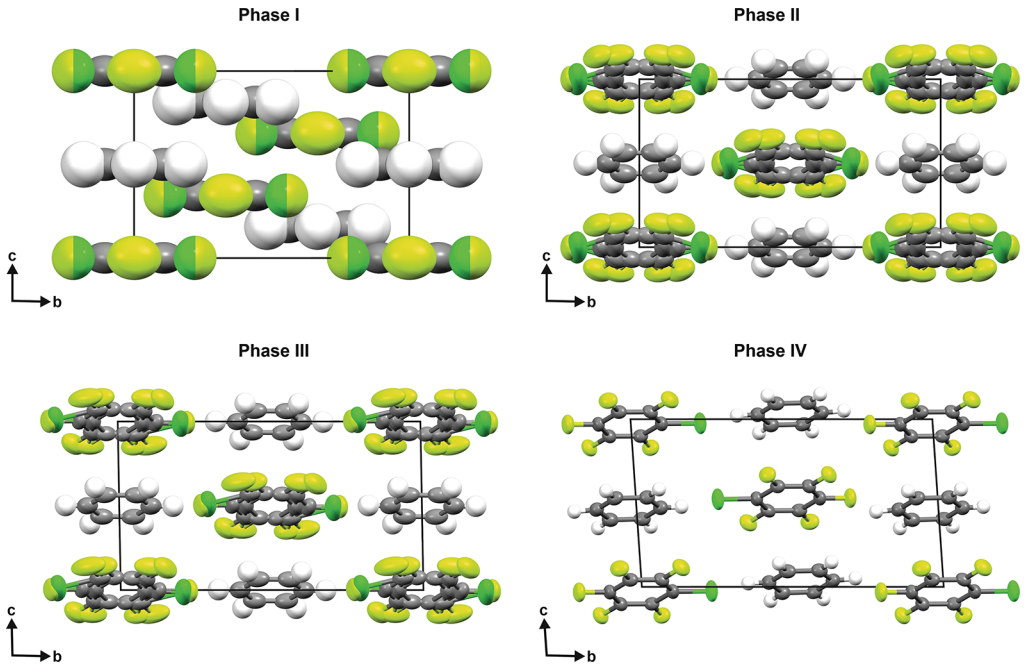

Figure 5. Views of the crystal structures of C_6H_6:C_6F_5Cl in phases I, II, III, and IV as for Figure 4 but now viewed along **a**. In this view, the alternating stacking of C_6H_6 and C_6F_5Cl molecules to form columns along **c** is readily seen as well as tilts of the planes of the molecules with respect to the column axis in phases II to IV.

capillary axis, as seen in the PXRD experiments.) However, the measurement of SXD data to high scattering angle is near impossible for a plastic phase given the very low intensity of the Bragg peaks at the higher (i.e., >60°) 2θ angles (as demonstrated *e.g.*, by the inset in Figure S4b, where a square root scale has been used to amplify the visibility of the weaker peaks of phase I seen in PXRD. Given that phase I is a plastic phase due to dynamic rotations, SXD data were not collected to the usual IUCr recommended limits (*i.e.* a *d*-spacing resolution of about 0.84 Å) as there are no measurable Bragg peaks at the higher 2θ angles.

Further details of the structure solution and refinement for phases I–IV of C_6H_6:C_6F_5Cl are given in the Supporting Information. The crystal structures of all four phases are shown in Figures 4 and 5; the naming of atoms is shown in Figure S6, and, along with the deposited CIF files, Tables S3–S6 provide details of the crystal structure parameters.

DISCUSSION

Our experimental work illustrates the importance of using multiple techniques for the study of the solid state. Although the crystal structures of all 4 solid-state phases of C_6H_6:C_6F_5Cl were solved and refined from SXD data, two of the phases would have been missed in the absence of the DSC and PXRD measurements: phase I because it only exists over a narrow range of temperature just below the melt and phase III because its unit cell is a small triclinic distortion of phase II, for which our current SXD acquisition software does not distinguish the difference easily. Furthermore, the DSC data was crucial in confirming the existence of four phases, especially given that one phase was missed in the initial PXRD experiment due to the use of a 10 K step size in temperature. Although 10 K steps are very practical in our X-ray laboratory (e.g., a typical VT-PXRD experiment can be run from late afternoon to the morning of the next day), there is always the risk (as we have seen in previous studies[33,45]) of accidently jumping over a phase that only exists over a narrow range of temperature. The study also illustrates the importance of analyzing the VT-PXRD prior to the SXD study. In particular, the indexing suite of programs within Crysfire2020[42] enabled us to identify the crystal systems and associated unit cells that we needed to measure in an SXD experiment.

An appreciation of the symmetry changes in the crystal on cooling (or heating) is equally important toward an understanding of the observed phase transitions. The symmetry elements present in the unit cells for all four phases may be seen in Figure S7. The change from phase I to phase II involves the loss of 3-fold symmetry so that the 6-fold disorder of the C_6F_5Cl molecules in phase I becomes just 2-fold disorder in phase II. The next change involves the loss of the mirror (and 2-fold) symmetry, but this still leaves the C_6F_5Cl molecules with 2-fold disorder (due to inversion symmetry). Hence, there is no appreciable change in volume at the II to III transition, just a small distortion of the unit cell with all cell angles no longer equal to 90°. Lastly, the III to IV transition involves a change from 2-fold disorder to antiferroelectric ordering of the C_6F_5Cl molecules that leads to a noticeable change in unit-cell volume. Although this transition can be described in terms of a change from a body-centered triclinic structure to a primitive triclinic one with half of the points of inversion being lost, it could equally well be described as a doubling of the primitive triclinic unit cell for phase III to the primitive triclinic unit cell for phase IV as a result of antiferroelectric ordering. Losing half of the points of inversion in phase III, and in particular the one at the origin where the C_6F_5Cl molecule is located, means that the structure of phase IV is best described in terms of a nonstandard setting of the triclinic space group with an origin defining inversion point at $(^1/_4,^1/_4,^1/_4)$.

The crystal structure refinements raise a number of interesting points. Despite the fact that C–Cl is a longer bond than C–F (1.704 Å versus 1.335 Å), when the structures

https://doi.org/10.1021/acs.cgd.4c00134
Cryst. Growth Des. 2024, 24, 3021–3029

Table 1. Comparison of the Space Groups, Temperature Ranges, and Structural Types for the Identified Solid-State Phases of the C_6H_6:C_6F_6, $C_6H_5CH_3$:C_6F_6 and C_6H_6:C_6F_5Cl Adducts[a]

adduct	space group symmetries and phases, temperature ranges, and types				
C_6H_6:C_6F_6	$R\bar{3}m$ (I)	$I2/m$ (II)	$P\bar{1}$ (III)		$P2_1/a$ (IV)
temperatures	297†−276 K	276−253 K	253−222* K		<222* K
order/disorder	plastic	ordered	ordered		ordered
$C_6H_5CH_3$:C_6F_6	$R\bar{3}m$ (I)		$I\bar{1}$ (II)	$P\bar{1}$ (III)	
temperatures	282 − 246 K		246−200	<200 K	
order/disorder:	plastic/6-fold		2-fold	A.F.	
C_6H_6:C_6F_5Cl	$R\bar{3}m$ (I)	$I2/m$ (II)	$I\bar{1}$ (III)	$P\bar{1}$ (IV)	
temperatures	266−244 K	244−190 K	190−160 K	<160 K	
order/disorder	plastic/6-fold	2-fold	2-fold	A.F.	

[a]Phases are denoted by the Roman numerals in parentheses, and temperature ranges are averaged from cooling and heating cycles using DSC. A.F. indicates an antiferroelectric structure; * indicates value from DSC heating cycle only, † is the melting-point value by Ripmeester *et al.*[46]

of phases II and III are refined with 2-fold disorder of the C_6F_5Cl molecule (using the tools in OLEX2[44]), the position of the Cl atom refines closer to the inversion center than the F atom opposite it in the C_6 ring (as seen in Figures 4 and 5). Attempts to model the disorder with Cl as the "outer" atom always resulted in it moving to the "inner" position. However, this result becomes less surprising when considering dynamic disorder and center-of-mass (CoM) distances: CoM···Cl(1) is equal to 2.81 versus 3.00 Å for CoM···F(4), both values calculated from the structure of phase IV in which the C_6F_5Cl molecule has an ordered orientation.

Phase transitions in this system gave rise to a few issues with regard to the use of the multigrain approach. The crystals of the lower-temperature phases exhibit twinning, not surprisingly, given the group−subgroup relationships between the phases. This was not a problem for phase II, perhaps because each twin domain is large enough to diffract just as one single crystal, but was a major issue by the time the crystals are cooled down to phase IV. Twinning in phase IV was obvious from the F_{obs} versus F_{calc} plot[44] of the refined structure; however, when the data for phase IV was processed subsequently as a twin, the completeness reduced to 94.6%. In addition, R_{int} was still relatively poor. Nonetheless, the structure of phase IV is considered reliable, with root-mean-square-plane deviation values of 0.005 and 0.001 Å for the rings in C_6F_5Cl and C_6H_6 (excl. H atoms), respectively.

By contrast, phase I presented other problems. First, the small number of unique reflections frequently landed the least-squares refinement in false minima. Second, relatively large crystals grow perfectly (i.e., with a low-mosaicity) just below the melt temperature, so an extinction correction is essential. (The use of an extinction correction for phase II can improve the *R*-factor, but its value was not significant.) Third, the very intense low-angle reflections are associated with large thermal diffuse scattering (see Figure S8), which may reduce their accuracy. Lastly, the data become exceedingly weak at the higher 2θ angles, which may be the cause of the relatively poor R_{int} values for this phase too, in contrast to the much better R_{int} values for phases II and III.

Finally, it is interesting to compare the solid-state behavior of the adduct C_6H_6:C_6F_5Cl with the prototype adduct C_6H_6:C_6F_6[32] and with the methyl-substituted adduct $C_6H_5CH_3$:C_6F_6.[33] The space-group symmetry for each of the phases is shown in Table 1.

All three show a high-temperature plastic phase with a rhombohedral arrangement of the molecules whose planes are perpendicular to the 3-fold symmetry axes in their crystal structures, in contrast to adducts formed by more highly substituted benzenes such as *p*-xylene and mesitylene.[19,33,41] The point symmetry of the molecules in phase II of C_6H_6:C_6F_5Cl is the same as for the molecules in C_6H_6:C_6F_6, namely $I2/m$, which results in 2-fold disorder for the C_6F_5Cl molecule as it lacks an inversion center. On further cooling of C_6H_6:C_6F_5Cl, the triclinic phase III is observed in which the C_6F_5Cl molecules still have 2-fold disorder. This phase is isomorphic to that observed in phase II of the toluene adduct which has 2-fold disorder of the $C_6H_5CH_3$ molecules. The structure of phase III of C_6H_6:C_6F_6 is very similar to these, especially when described in terms of an *I*-centered triclinic unit cell. Lastly, at the lowest temperature, the C_6F_5Cl molecules undergo antiferroelectric ordering, leading to the primitive triclinic phase IV, isomorphic to phase III of the toluene adduct. In phase IV, the molecules show an eclipsed arrangement as seen in phases III of C_6H_6:C_6F_6 and $C_6H_5CH_3$:C_6F_6, and in the lowest temperature phase of *p*-$C_6H_4(CH_3)_2$:C_6F_6.[33] Thus, C_6H_6:C_6F_5Cl behaves like $C_6H_5CH_3$:C_6F_6 with the key difference being the existence of monoclinic phase II in the former. We note that a transient minor phase was observed in the latter in a VT-PXRD experiment using 1 K steps around the I−II phase transition. We speculate that this minor phase, for which there were insufficient peaks for indexing, might be equivalent to the extra phase II seen in C_6H_6:C_6F_5Cl. The existence of the extra phase II in C_6H_6:C_6F_5Cl can be rationalized in terms of the high degree of molecular motion (as deduced from the atomic displacement parameters) of the C_6F_5Cl molecules, which leads to dynamic disorder of the Cl atom away from the 2-fold axis. However, the data does not sustain modeling this phase with a higher degree of disorder than the 2-fold one used.

It has been postulated that the structure of this type of adduct from the melt is determined by the attraction of opposing quadrupole forces.[31] The formation of columns of alternating molecules, which are dynamically disordered and aligned along an axis perpendicular to their plane, bears this out, as the quadrupole and molecular dipole of the C_6F_5Cl molecules are the sole directional forces in this system even though they are not the largest contributor toward the overall energy of the system.[47] We note that precise experimental values for the quadrupole and molecular dipole of the C_6F_5Cl

https://doi.org/10.1021/acs.cgd.4c00134
Cryst. Growth Des. 2024, 24, 3021−3029

molecule appear to be unknown. In contrast to C_6H_6:C_6F_6, but in comparison with $C_6H_5CH_3$:C_6F_6, the molecular dipole moment plays an additional role, particularly at low temperature, as it results in antiferroelectric ordering in phase IV.

In addition, molecular bond-dipole interactions (*i.e.* C−F···H−C)[48] have a role to play in determining whether the molecules with opposite quadrupole moments are staggered or eclipsed.[33] The relative strength of these interactions is most evident when the lowest temperature phase IV is compared with the highest temperature phase I. Despite the very weak nature of these interactions, in the absence of any stronger directional forces, the bond−dipole forces in phase IV lead to the eclipsed arrangement of molecules within a column. In addition, the molecules tilt within a column so as to maximize the intercolumnar interactions (Figure S9). Not only do the molecules tilt with respect to the column axis (Figure 5), but they are also very slightly tilted with respect to each other, with an interplanar angle between adjacent C_6H_6 and C_6F_5Cl molecules within a column equal to 3.26°. By contrast, near the melt, the strong librational motion of the molecules results in weak intercolumnar interactions and leads to molecules aligned perfectly parallel to each other with an interplanar angle between molecules within a column equal to 0°.

In our previous work on cocrystals involving C_6F_6, we observed that, despite preparing 1:1 stoichiometric mixtures, occasionally a cocrystal formed that was not in a 1:1 stoichiometry, e.g., the cocrystals formed C_6F_6 and C_4H_5N crystallized with the unusual formula $(C_6F_6)_3$:$(C_4H_5N)_4$.[19] Until the crystal structure is solved, it is difficult to predict the ratio of coformers in the cocrystal. In this work, we were attempting to assemble a cocrystal with columns of molecules composed of alternating coformers that naturally leads to a 1:1 stoichiometry. In the aforementioned work of Bujak et al. on the cocrystal of C_6H_6 with C_6F_5I,[40] it is not obvious why a 1:2 ratio of coformers was chosen *prior* to structure solution other than a cocrystal of C_6H_6 and CF_3I had been formed previously in this ratio.[39]

Despite the different stoichiometries observed between C_6H_6:C_6F_5Cl and C_6H_6:$(C_6F_5I)_2$, the solid-state structures share a number of features in common. The crystal structures of all forms of both have the molecules arranged in columns and exhibit phase transitions to low symmetry forms on cooling. In particular, the monoclinic to triclinic transition in C_6H_6:$(C_6F_5I)_2$ is similar to the II to III transition in C_6H_6:C_6F_5Cl. However, there are number of differences associated with the different stoichiometries. In the lowest-temperature form of C_6H_6:C_6F_5Cl, the C_6F_5Cl molecules are aligned with the dipoles opposed between columns (Figure 5) but not along the column axis in contrast to the C_6F_5I molecules in C_6H_6:$(C_6F_5I)_2$ where the dipoles of the C_6F_5I molecules are opposed within the column (Figure S1), thus leading to a structure with a 1:2 stoichiometry. Finally, we note that only two solid-state phases were reported for C_6H_6:$(C_6F_5I)_2$ whereas C_6H_6:C_6F_5Cl exhibits four.

CONCLUSIONS

In this study, it is evident that fluorine substitution by chlorine in C_6F_6 does indeed perturb the structure and dynamics of the prototype adduct C_6H_6:C_6F_6, in a number of ways. First, compared to C_6H_6:C_6F_6, the plastic phase just below the melt exists over a much narrower range of temperature in C_6H_6:C_6F_5Cl. Second, C_6H_6:C_6F_5Cl retains the analogous "extreme" phases shown by $C_6H_5CH_3$:C_6F_6, namely, the plastic high-temperature phase and the antiferroelectric low-temperature phase. Third, in contrast with $C_6H_5CH_3$:C_6F_6, but similar to the prototype, C_6H_6:C_6F_5Cl also has an intermediate monoclinic phase. Using a combination of DSC, VT-PXRD, and SXD, we have shown that the adduct formed between C_6H_6 and C_6F_5Cl has four solid-state phases at low temperature.

Currently, CSP cannot predict the phase behavior of simple adducts such as C_6H_6:C_6F_5Cl and similar systems. These systems tend to exhibit many phases where the energy difference between phases is relatively small and comparable to the energy differences between structures predicted by CSP. Detailed experimental investigations as described in this paper highlight and scrutinize some of the fundamental weak interactions that hold molecules together in solid materials. For example, DSC measurements show that the energy differences between phases are small, especially for a subtle phase change such as the II−III transition in this system, where ΔH is about ±0.3 kJ mol^{-1}. This implies that those developing CSP methods and protocols need to calculate lattice energies to a higher accuracy in order to more effectively predict the phase behavior of some simple organic molecules. The studies presented here will be useful in informing future predictive studies and provide essential data for developing and training models for CSP.

The findings herein have led us to postulate further questions, such as how does further perturbation of the prototype adduct (C_6H_6:C_6F_6), *e.g.*, by both hydrogen and fluorine substitutions in each ring to create an adduct such as $C_6H_5CH_3$:C_6F_6Cl, where both coformers have a molecular dipole, affect the structure and dynamics of the system?

ASSOCIATED CONTENT

Supporting Information

The Supporting Information is available free of charge at https://pubs.acs.org/doi/10.1021/acs.cgd.4c00134.

Additional experimental details, crystallographic tables, and additional supporting figures (PDF)

Accession Codes

CCDC 2327945−2327948 contain the supplementary crystallographic data for this paper. These data can be obtained free of charge via www.ccdc.cam.ac.uk/data_request/cif, or by emailing data_request@ccdc.cam.ac.uk, or by contacting The Cambridge Crystallographic Data Centre, 12 Union Road, Cambridge CB2 1EZ, UK; fax: +44 1223 336033.

AUTHOR INFORMATION

Corresponding Author

Jeremy K. Cockcroft − *Department of Chemistry, Christopher Ingold Laboratories, University College London, London WC1H 0AJ, United Kingdom;* orcid.org/0000-0002-4954-651X; Email: j.k.cockcroft@ucl.ac.uk

Authors

Joseph C. Bear − *School of Life Sciences, Pharmacy and Chemistry, Kingston University, Kingston upon Thames KT1 2EE, United Kingdom;* orcid.org/0000-0001-6504-4723

Ronen E. Ghosh − *Department of Chemistry, Christopher Ingold Laboratories, University College London, London WC1H 0AJ, United Kingdom*

Complete contact information is available at: https://pubs.acs.org/10.1021/acs.cgd.4c00134

https://doi.org/10.1021/acs.cgd.4c00134
Cryst. Growth Des. 2024, 24, 3021−3029

Author Contributions

The manuscript was written through contributions from all authors. All authors have given approval to the final version of the manuscript.

Funding

We acknowledge financial support from the U.K. Engineering and Physical Sciences Research Council for funding the X-ray diffractometers (grant reference EP/K03930X/1).

Notes

The authors declare no competing financial interest.

■ ACKNOWLEDGMENTS

We thank Dr. Alexander Rosu-Finsen and Prof. Christoph G. Salzmann for help with data collection using their low-temperature DSC calorimeter and Mr. Martin Vickers for his freely given help in the repair of the Oxford Instruments CryojetHT that was used in the VT-PXRD experiments.

■ ABBREVIATIONS

ACA, American Crystallographic Association; BCA, British Crystallographic Association; CCDC, Cambridge Crystallographic Data Centre; CSP, crystal structure prediction; DSC, differential scanning calorimetry; IUCr, International Union of Crystallography; VT-PXRD, variable-temperature powder X-ray diffraction; SXD, single-crystal X-ray diffraction

■ REFERENCES

(1) Lommerse, J. P. M.; Motherwell, W. D. S.; Ammon, H. L.; Dunitz, J. D.; Gavezzotti, A.; Hofmann, D. W. M.; Leusen, F. J. J.; Mooij, W. T. M.; Price, S. L.; Schweizer, B.; et al. A Test of Crystal Structure Prediction of Small Organic Molecules. *Acta Crystallogr., Sect. B: Struct. Sci.* **2000**, *56*, 697−714.

(2) Reilly, A. M.; Cooper, R. I.; Adjiman, C. S.; Bhattacharya, S.; Boese, A. D.; Brandenburg, J. G.; Bygrave, P. J.; Bylsma, R.; Campbell, J. E.; Car, R.; et al. Report on the Sixth Blind Test of Organic Crystal Structure Prediction Methods. *Acta Crystallogr., Sect. B: Struct. Sci., Cryst. Eng. Mater.* **2016**, *72*, 439−459.

(3) (a) Hunnisett, L.; Cole, J.; Sadiq, G. What Have We Learned From the Seventh Blind Test of Crystal Structure Prediction? — Triumphs, Challenges, and Insights. *Acta Crystallogr., Sect. A: Found. Adv.* **2022**, *A78*, No. a136. (b) Hunnisett, L. The CCDC Blind Tests: Showcasing the triumphs, challenges, and evolution of Crystal Structure Prediction. *Crystallogr. News* **2022**, *163*, 9. (c) Hunnisett, L. M.; Nyman, J.; Francia, N.; Sadiq, G.; Sugden, I.; Reutzel-Edens, S.; Cole, J. A Seventh Blind Test of Crystal Structure Prediction Methods. *Acta Crystallogr., Sect. A: Found. Adv.* **2024**.

(4) Xu, Y.; Marrett, J. M.; Titi, H. M.; Darby, J. P.; Morris, A. J.; Friščić, T.; Arhangelskis, M. Experimentally Validated Ab Initio Crystal Structure Prediction of Novel Metal−Organic Framework Materials. *J. Am. Chem. Soc.* **2023**, *145*, 3515−3525.

(5) Yang, J.; De, S.; Campbell, J. E.; Li, S.; Ceriotti, M.; Day, G. M. Large-Scale Computational Screening of Molecular Organic Semiconductors Using Crystal Structure Prediction. *Chem. Mater.* **2018**, *30*, 4361−4371.

(6) Beran, G. J. O. Frontiers of Molecular Crystal Structure Prediction for Pharmaceuticals and Functional Organic Materials. *Chem. Sci.* **2023**, *14*, 13290.

(7) Corpinot, M. K.; Bucar, K. A Practical Guide to the Design of Molecular Crystals. *Cryst. Growth Des.* **2019**, *19*, 1426−1453.

(8) Nyman, J.; Day, G. M. Static and Lattice Vibrational Energy Differences between Polymorphs. *CrystEngComm* **2015**, *17*, 5154−5165.

(9) Cruz-Cabeza, A. J.; Reutzel-Edens, S. M.; Bernstein, J. Facts and Fictions about Polymorphism. *Chem. Soc. Rev.* **2015**, *44*, 8619−8635.

(10) Yang, M.; Dybeck, E.; Sun, G.; Peng, C.; Samas, B.; Burger, V. M.; Zeng, Q.; Jin, Y.; Bellucci, M. A.; Liu, Y.; et al. Prediction of the Relative Free Energies of Drug Polymorphs above Zero Kelvin. *Cryst. Growth Des.* **2020**, *20*, 5211−5224.

(11) Nikhar, R.; Szalewicz, K. Reliable Crystal Structure Predictions from First Principles. *Nat. Commun.* **2022**, *13*, 3095.

(12) McDonagh, D.; Skylaris, C.-K.; Day, G. M. Machine-Learned Fragment-Based Energies for Crystal Structure Prediction. *J. Chem. Theory Comput.* **2019**, *15*, 2743−2758.

(13) Hoja, J.; Ko, H.-Y.; Neumann, M. A.; Car, R.; DiStasio, R. A., Jr.; Tkatchenko, A. Reliable and Practical Computational Description of Molecular Crystal Polymorphs. *Sci. Adv.* **2019**, *5*, eaau3338.

(14) Nyman, J.; Day, G. M. Modelling Temperature-Dependent Properties of Polymorphic Organic Molecular Crystals. *Phys. Chem. Chem. Phys.* **2016**, *18*, 31132−31143.

(15) Carpenter, J. E.; Grünwald, M. Pre-Nucleation Clusters Predict Crystal Structures in Models of Chiral Molecules. *J. Am. Chem. Soc.* **2021**, *143*, 21580−21593.

(16) Kruglov, I. A.; Yanilkin, A. V.; Propad, Y.; Mazitov, A. B.; Rachitskii, P.; Oganov, A. R. Crystal Structure Prediction at Finite Temperatures. *NPJ Comput. Mater.* **2023**, *9*, 197.

(17) Groom, C. R.; Allen, F. H. The Cambridge Structural Database in Retrospect and Prospect. *Angew. Chem., Int. Ed.* **2014**, *53*, 662−671.

(18) Ward, S. C.; Sadiq, G. Introduction to the Cambridge Structural Database − a Wealth of Knowledge Gained from a Million Structures. *CrystEngComm* **2020**, *22*, 7143−7144.

(19) Bear, J. C.; Terzoudis, N.; Cockcroft, J. K. Single-Crystal Quality Data from Polycrystalline Samples: Finding the Needle in the Haystack. *IUCrJ.* **2023**, *10*, 720−728.

(20) Patrick, C. R.; Prosser, G. S. A Molecular Complex of Benzene and Hexafluorobenzene. *Nature* **1960**, *187*, 1021−1021.

(21) Otero-de-la-Roza, A.; Johnson, E. R. A Benchmark for Non-Covalent Interactions in Solids. *J. Chem. Phys.* **2012**, *137*, No. 054103.

(22) Stevens, J. S.; Seabourne, C. R.; Jaye, C.; Fischer, D. A.; Scott, A. J.; Schroeder, S. L. M. Incisive Probing of Intermolecular Interactions in Molecular Crystals: Core Level Spectroscopy Combined with Density Functional Theory. *J. Phys. Chem. B* **2014**, *118*, 12121−12129.

(23) Legon, A. C. The Halogen Bond: an Interim Perspective. *Phys. Chem. Chem. Phys.* **2010**, *12*, 7736−7747.

(24) Cavallo, G.; Metrangolo, P.; Milani, R.; Pilati, T.; Priimagi, A.; Resnati, G.; Terraneo, G. The Halogen Bond. *Chem. Rev.* **2016**, *116*, 2478−2601.

(25) Mahmudov, K. T.; Pombeiro, A. J. L. 1st International Conference on Noncovalent Interactions. *New J. Chem.* **2019**, *43*, 13312−13314.

(26) Dahl, T.; Gropen, O.; Wilhelmi, K. A.; Lindberg, A. A.; Lagerlund, I.; Ehrenberg, L. Crystal Structure of the 1:1 Complex Between Mesitylene and Hexafluorobenzene. *Acta Chem. Scand.* **1971**, *25*, 1031−1039.

(27) Dahl, T.; Klæboe, P.; Tucker, E. E.; Songstad, J.; Svensson, S. Crystal Structure of the Trigonal Form of the 1:1 Complex Between Hexamethylbenzene and Hexafluorobenzene. *Acta Chem. Scand.* **1972**, *26*, 1569−1575.

(28) Dahl, T. Crystal Structure of the 1:1 Addition Compound Between *p*-Xylene and Hexafluorobenzene. *Acta Chem. Scand., Ser. A* **1975**, *29*, 170−174.

(29) Williams, J. H.; Cockcroft, J. K.; Fitch, A. N. Structure of the Lowest Temperature Phase of the Solid Benzene-Hexafluorobenzene Adduct. *Angew. Chem., Int. Ed. Engl.* **1992**, *31*, 1655−1657.

(30) Steed, J. M.; Dixon, T. A.; Klemperer, W. Molecular Beam Studies of Benzene Dimer, Hexafluorobenzene Dimer, and Benzene−Hexafluorobenzene. *J. Chem. Phys.* **1979**, *70*, 4940−4946.

(31) Williams, J. H. The Molecular Electric Quadrupole Moment and Solid-State Architecture. *Acc. Chem. Res.* **1993**, *26*, 593−598.

(32) Cockcroft, J. K.; Rosu-Finsen, A.; Fitch, A. N.; Williams, J. H. The Temperature Dependence of C−H···F−C Interactions in Benzene:Hexafluorobenzene. *CrystEngComm* **2018**, *20*, 6677−6682.

https://doi.org/10.1021/acs.cgd.4c00134
Cryst. Growth Des. 2024, 24, 3021−3029

(33) Cockcroft, J. K.; Li, J. G. Y.; Williams, J. H. Influence of Methyl-Substitution on the Dynamics of the C−H···F−C Interaction in Binary Adducts. *CrystEngComm* **2019**, *21*, 5578−5585.
(34) Bear, J. C.; Cockcroft, J. K.; Williams, J. H. Influence of Solvent in Crystal Engineering: A Significant Change to the Order−Disorder Transition in Ferrocene. *J. Am. Chem. Soc.* **2020**, *142*, 1731−1734.
(35) Sherwood, J. N. (Ed.) *The Plastically Crystalline State: Orientationally Disordered Crystals*. Wiley: New York. 1979, 1−383.
(36) (a) Price, S. L. Is Zeroth Order Crystal Structure Prediction (CSP_0) Coming to Maturity? What Should We Aim for in an Ideal Crystal Structure Prediction Code? *Faraday Discuss.* **2018**, *211*, 9−30. (b) Ruggiero, M. T.; Kölbel, J.; Li, Q.; Zeitler, J. A. Predicting the Structures and Associated Phase Transition Mechanisms in Disordered Crystals *via* a Combination of Experimental and Theoretical Methods. *Faraday Discuss.* **2018**, *211*, 425−439.
(37) Pang, X.; Wang, H.; Wang, W.; Jin, W. J. Phosphorescent π-Hole···π Bonding Cocrystals of Pyrene with Haloperfluorobenzenes (F, Cl, Br, I). *Cryst. Growth Des.* **2015**, *15*, 4938−4945.
(38) Rozhkov, A. V.; Krykova, M. A.; Ivanov, D. M.; Novikov, A. S.; Sinelshchikova, A. A.; Volostnykh, M. V.; Konovalov, M. A.; Grigoriev, M. S.; Gorbunova, Y. G.; Kukushkin, V. Y. Reverse Arene Sandwich Structures Based upon π-Hole···[M^{II}] (d^8 M = Pt, Pd) Interactions, where Positively Charged Metal Centers Play the Role of a Nucleophile. *Angew. Chem., Int. Ed.* **2019**, *58*, 4164−4168.
(39) Bujak, M.; Stammler, H.-G.; Blomeyer, S.; Mitzel, N. W. The Nature of Interactions of Benzene with CF_3I and CF_3CH_2I. *Chem. Commun.* **2019**, *55*, 175−178.
(40) Bujak, M.; Stammler, H.-G.; Mitzel, N. W. Molecules Forced to Interact: Benzene and Pentafluoroiodobenzene. *Cryst. Growth Des.* **2020**, *20*, 3217−3223.
(41) Cockcroft, J. K.; Ghosh, R. E.; Shephard, J. J.; Singh, A.; Williams, J. H. Investigation of the Phase Behaviour of the 1:1 Adduct of Mesitylene and Hexafluorobenzene. *CrystEngComm* **2017**, *19*, 1019−1023.
(42) (a) Bergmann, J.; Le Bail, A.; Shirley, R.; Zlokazov, V. Renewed Interest in Powder Diffraction Data Indexing. *Z. Kristallogr.* **2004**, *219*, 783−790. (b) Ghosh, R. E. *Crysfire2020 Aids Indexing Powder Diffraction Peak Data*. http://ccp14.cryst.bbk.ac.uk/Crysfire.html.
(43) Le Bail, A.; Duroy, H.; Fourquet, J. L. Ab-Initio Structure Determination of $LiSbWO_6$ by X-ray Powder Diffraction. *Mater. Res. Bull.* **1988**, *23*, 447−452.
(44) Dolomanov, O. V.; Bourhis, L. J.; Gildea, R. J.; Howard, J. A. K.; Puschmann, H. OLEX2: a Complete Structure Solution, Refinement and Analysis Program. *J. Appl. Crystallogr.* **2009**, *42*, 339−341.
(45) Cockcroft, J. K.; Shamsabadi, A.; Wu, H.; Rennie, A. R. Understanding the Structure and Dynamics of Cationic Surfactants from Studies of Pure Solid Phases. *Phys. Chem. Chem. Phys.* **2019**, *21*, 25945−25951.
(46) Ripmeester, J. A.; Wright, D. A.; Fyfe, C. A.; Boyd, R. K. Molecular Motion and Phase Transitions in Solid Hexafluorobenzene +Benzene Complex by Nuclear Magnetic Resonance and Heat Capacity Measurements. *J. Chem. Soc., Faraday Trans. 2* **1978**, *74*, 1164−1178.
(47) Otero-de-la-Roza, A.; Johnson, E. R.; Contreras-García, J. Revealing Non-covalent Interactions in Solids: NCI Plots Revisited. *Phys. Chem. Chem. Phys.* **2012**, *14*, 12165−12172.
(48) Thalladi, V. R.; Weiss, H.-C.; Bläser, D.; Boese, R.; Nangia, A.; Desiraju, G. R. C−H···F Interactions in the Crystal Structures of Some Fluorobenzenes. *J. Am. Chem. Soc.* **1998**, *120*, 8702−8710.

https://doi.org/10.1021/acs.cgd.4c00134
Cryst. Growth Des. 2024, 24, 3021−3029